Strain-dependent near-zero and negative Poisson ratios in a two-dimensional $(CuI)P_4Se_4$ monolayer

Wenjiang Gao,[1] Xiaobo Shi,[1,2] Yusen Qiao,[1] Meiyang Yu,[1] and Huabing Yin[1,*]

[1]*Institute for Computational Materials Science, Joint Center for Theoretical Physics, and International Joint Research Laboratory of New Energy Materials and Devices of Henan Province, School of Physics and Electronics, Henan University, Kaifeng 475004, China*

[2]*School of Computer and Artificial Intelligence, Henan Finance University, Zhengzhou 450046, China*

(Received 16 November 2023; revised 9 January 2024; accepted 16 January 2024; published 1 February 2024)

The unique mechanical properties of auxetic materials are widely used in specialized fields, such as medicine, defense security, and aerospace. Here, a potential two-dimensional (2D) auxetic $(CuI)P_4Se_4$ material is predicted by first-principles calculations. The 2D $(CuI)P_4Se_4$ monolayer is a quasidirect-band-gap semiconductor with a relatively large band gap of 2.66 eV, which can be regulated by applying uniaxial strain. In particular, the unique coordinate structure of polymeric P_4Se_4 strands and Cu_2I_2 units endows the $(CuI)P_4Se_4$ monolayer with fascinating mechanical flexibility and anisotropy. The calculated Young's modulus of 8.62 (41.81) N/m and ideal fracture strength 0.66 (1.35) N/m in the x (y) direction are one to two orders of magnitude smaller than those of other previously reported 2D materials. More remarkably, the $(CuI)P_4Se_4$ monolayer exhibits the strain-dependent near-zero Poisson's ratio (ZPR) and negative Poisson's ratio (NPR) behaviors. Both the in-plane and out-of-plane Poisson's ratios can translate from positive value to negative value under suitable in-plane uniaxial strain. Our calculations show that the in-plane NPR characteristic is mainly controlled by the distances and angles of the neighbor Cu atoms and the out-of-plane NPR behavior is mainly dominated by the rotation of Cu_2I_2 units. In addition, the electronic and geometric response analyses further determine that the difference of strain-response capabilities between P_4Se_4 strands and Cu_2I_2 units should be responsible for the strain-dependent mechanical properties. Our results reveal a 2D intrinsic near ZPR and NPR material $(CuI)P_4Se_4$ and explore the origin of its strain-dependent mechanical behaviors.

DOI: 10.1103/PhysRevB.109.075402

I. INTRODUCTION

Poisson's ratio (υ) and Young's modulus (Y) are both inherent properties of materials and important parameters for judging the mechanical properties of materials. Poisson's ratio refers to the deformation response in relaxable cross direction(s) of the material under orthogonal strain, which is usually affected by the crystal structure and electronic properties [1–5]. According to classical elastic theory, the Poisson's ratio of three-dimensional (3D) materials can be between -1 and 0.5 [6]. In this way, materials can be divided into three types according to the value of Poisson's ratio, positive Poisson's ratio (PPR), zero Poisson's ratio (ZPR), and negative Poisson's ratio (NPR) materials. When the value of Poisson's ratio is positive, it shows that the material will contract (expand) laterally when stretched (compressed) lengthwise. However, when the value of Poisson's ratio is negative, the material exhibits transverse expansion (contraction) when lengthwise stretching (compression) is applied. This captivating auxetic effect distinguishes these materials, giving rise to their classification as auxetic materials. In addition, when the value of Poisson's ratio is zero, it shows a uniaxial-strain-insensitive characteristic. However, the Poisson's ratio of materials exactly equal to zero are very rare, thus, the materials with near ZPR ($|\upsilon| < 0.01$) have also received more attention [7,8]. Previous works reported that the crystal structures and electronic properties of the materials will change under the strain conditions [5,8,9]. This will lead to the variation of Poisson's ratio. Therefore, the mechanical responses of materials under certain strain ranges should be carefully considered.

In general, the materials with PPR are common. However, the materials with NPR and ZPR are relatively scarce. In particular, the NPR materials may exhibit the enhanced mechanical properties, including fracture toughness, shear resistance, vibration absorption, and acoustic absorption [10,11]. For example, the shear resistance is inversely proportional to $(1 + \upsilon)$. Thus, when Poisson's ratio is infinitely close to the extreme value -1, the shear resistance will be greatly enhanced and even tend to infinity. Due to the intriguing mechanical properties, NPR materials have great application potential in many fields, such as defense, medicine, automotive industries, and aerospace [12–15]. By contrast, the ZPR materials have a negligible deformation response, which can reduce the stress and shape change when the strain is applied. Hence, the ZPR materials can be used for skins, sealing, and morphing aircraft [16,17]. The widely known near ZPR materials are gas, cork, and spongy graphene [18,19]. Recent studies show that it is possible to transform PPR or NPR materials into ZPR materials by means of strain [8,20].

In fact, various auxetic 3D and two-dimensional (2D) lattices have been proposed and the origin of NPR in these auxetic lattices has been theoretically analyzed from the

*yhb@henu.edu.cn

nanoscale or microscopic structure [21–29]. For example, Alderson *et al.* proposed the rotation and dilation deformation mechanisms for auxetic behavior in the tetrahedral framework structures [21–23]. They have shown that both concurrent tetrahedral rotation and dilation are needed to explain both the PPR and NPR in these α-quartz and α-cristobalite molecular tetrahedral frameworks. Cabras *et al.* also proposed several classes of 3D and 2D lattice structures with macroscopic NPR [26–28]. Such lattice structures have an omnidirectional NPR close to the stability limit -1. Evans *et al.* also studied the 2D auxetic polymer networks using molecular modeling and analytical modeling techniques. These 2D polymer networks have conventional and reentrant honeycomb forms. They suggested that the NPR behavior within polymer networks stemmed from the deformation of networks through a combination of hinging, flexure, and stretching of the honeycomb cell walls [29]. These previous theoretical studies about the 2D and 3D auxetic lattices can help us to know the auxetic mechanism in practical materials.

In the past few decades, the low-dimensional material systems have been rapidly developed [30–36]. Remarkably, a lot of 2D materials with excellent chemical and physical properties have been reported, such as graphene [32,37,38], phosphorene [39,40], and transition metal dichalcogenides (TMDs) [41,42]. Based on the continuous discovery of 3D materials with NPR and ZPR [1,2,43–46], people turn their attention to 2D materials, hoping to find NPR and ZPR behaviors in 2D materials. After continuous research and development, some 2D NPR materials have been recently reported [5,8,9,47–49]. Examples mainly include graphene [5], black phosphorus [50], Me-graphene [8], Ag_2S [47], WN_4 [49], and R-Cu_2Se_2 [9]. At the same time, most 2D NPR materials exhibit the Poisson's ratio transition behavior under strain [5,8]. In addition, there are different explanations for the existence of NPR and ZPR in 2D materials [5,8,9,47–50]. For example, Jin *et al.* found that the NPR behavior in 2D WN_4 is attributed to the fourfold-coordinated WN_4 tetrahedron combined with the strong coupling between the $2p$ orbitals of N and $5d$ orbitals of W, which is a synergistic effect of electronic and structural properties [49]. Qin *et al.* studied the NPR behavior in 2D graphene under strain, and proposed that the NPR behavior under strain was caused by electron localization function (ELF) coupling [5]. Yu *et al.* report that the emerging NPR in 2D *R*-Cu_2Se_2 is attributed to the weak electronegativity of Se atoms under multiorbital hybridization, which is the strong strain response of interlayer interaction driven by electron effects [9]. Thus, exploring new 2D NPR and ZPR materials and investigating the property origin are still the key areas of concern.

As reaction media, copper halides (CuI) can readily incorporate group-V and -VI low-charged molecules to form adduct compounds [51–54]. For example, bulk (CuI)P_4Se_4, which was a typical van der Waals (vdW) layer material, was synthesized through the reaction of CuI, red P, and gray Se in 1999 [54]. In each layer, the polymeric P_4Se_4 strands were connected with [Cu_2I_2] units. Due to the flexibility of the bond angles I-Cu-I and Cu-I-Cu, the rhomboid arrangement can be squeezed along the I-I and Cu-Cu axes. Such special geometrical structure may endow the (CuI)P_4Se_4 layer with promising mechanical properties.

In this work, we predict a 2D monolayer material, (CuI)P_4Se_4, based on the first-principles methods. Our results show that the (CuI)P_4Se_4 monolayer can be exfoliated from its bulk counterpart and remains stable at room temperature. At the same time, the (CuI)P_4Se_4 monolayer has a relatively large band gap of 2.66 eV. Interestingly, the Young's modulus and ideal tensile strength of the (CuI)P_4Se_4 monolayer are much lower than those of most reported 2D materials, indicating its promising mechanical flexibility. Due to its special structure, the (CuI)P_4Se_4 monolayer exhibits the strain-dependent NPR and near ZPR behaviors in the in-plane and out-of-plane directions. Then, using geometric structure and electronic response methods, we study and trace the source of the NPR and near ZPR. The differences of strain-response capabilities between the P_4Se_4 and Cu_2I_2 units are crucial to the strain-dependent NPR and near ZPR characteristics in the (CuI)P_4Se_4 monolayer. The outstanding mechanical responses of the (CuI)P_4Se_4 monolayer are conducive to its application in the field of highly flexible and multifunctional devices.

II. COMPUTATIONAL METHODS

All first-principles calculations in this work were based on density functional theory (DFT) as implemented in the Vienna *ab initio* simulation package (VASP) [55,56]. The generalized gradient approximation (GGA) with Perdew-Burke-Ernzerhof (PBE) method was applied for the exchange-correlation functional [57]. The projected augmented wave (PAW) method was used to account for the electron-ion interactions [58]. The kinetic cutoff energy is set to 550 eV for the plane-wave basis in all calculations. The Brillouin zone was sampled using grid sizes of $6 \times 5 \times 1$ in the Γ-centered **k**-points scheme [59]. A vacuum space with a thickness of 25 Å along the z direction was added to minimize the interaction between the periodic images. The convergence criteria for the energy and force were set as 10^{-8} eV and 10^{-3} eV/Å, respectively. The electronic structure was calculated based on Heyd-Scuseria-Ernzerhof (HSE06) hybrid functional [60]. The vdW interaction was described by the DFT-D3 method [61]. The finite displacement method was used to calculate the phonon spectrum, which implemented in the PHONOPY code with a $2 \times 2 \times 1$ supercell [62]. Also, *ab initio* molecular dynamics (AIMD) simulation was carried out on the same $2 \times 2 \times 1$ supercell and the temperature was kept at 300 K by using a canonical NVT ensemble [63,64]. The VASPKIT package was used for postprocessing [65]. The VESTA software was used for the visualizations of structure [66]. The strength of chemical bonds is analyzed by crystal orbital Hamilton population (COHP) method [67,68], implemented in the LOBSTER code [69].

III. RESULTS AND DISCUSSION

A. Structure and stability

Bulk (CuI)P_4Se_4, synthesized experimentally in 1999, is a vdW-layer adduct compound with *Cmca* (No. 64) space group [54]. Each layer is consisted of polymeric P_4Se_4 strands connected with Cu_2I_2 units. The neutral polymeric P_4Se_4 strands consist of norbornane analogous P_4Se_3 units which

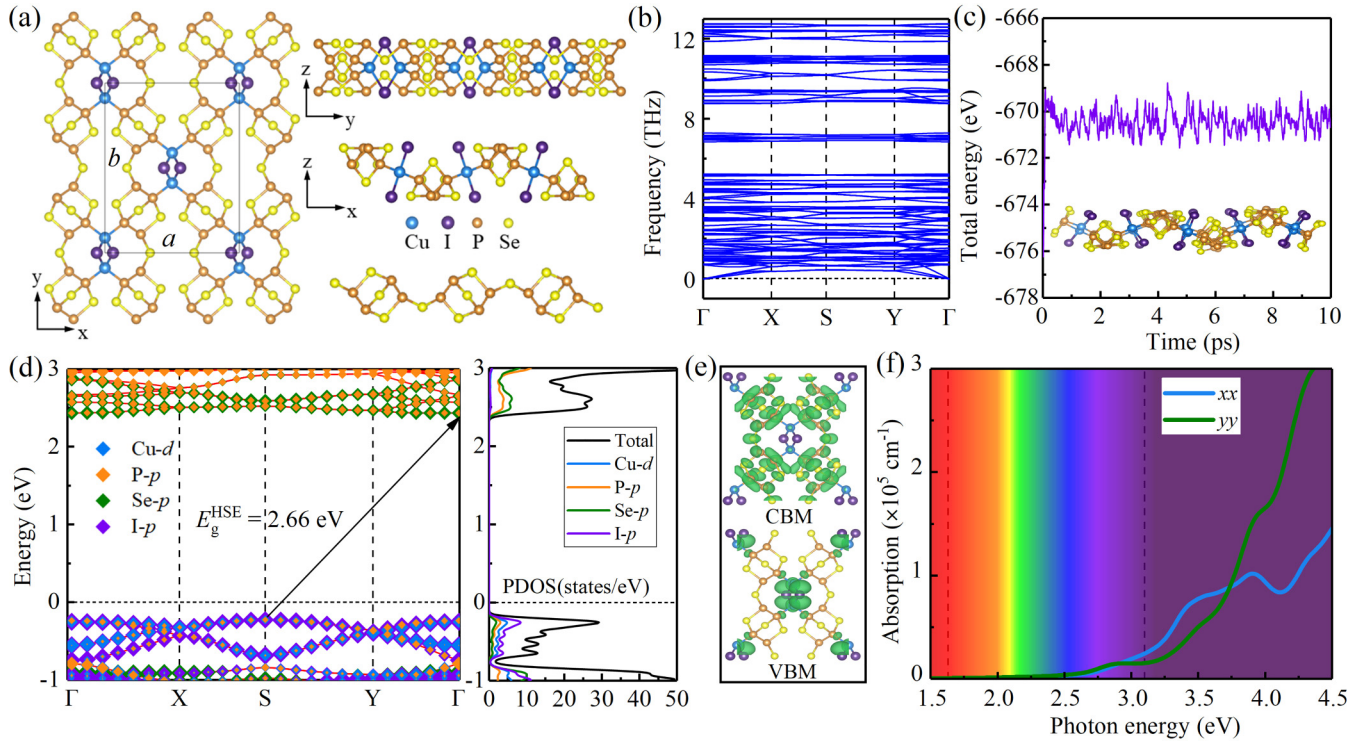

FIG. 1. (a) The optimized structures of the $(CuI)P_4Se_4$ monolayer. The *a* and *b* represent the corresponding lattice constants. (b) Phonon spectrum of the $(CuI)P_4Se_4$ monolayer. (c) The fluctuation of total energy of the $(CuI)P_4Se_4$ monolayer during the AIMD simulation at 300 K. The insets show the atomic structure at the end of the simulation. (d) The projected band structures and partial density of states (PDOS) of the $(CuI)P_4Se_4$ monolayer calculated by the HSE06 functional. The Fermi level is set at zero. (e) Electron density distributions of the CBM and VBM for the $(CuI)P_4Se_4$ monolayer. (f) Optical absorption coefficients of the $(CuI)P_4Se_4$ monolayer calculated by the HSE06 functional.

are linked by Se atoms. The P_4Se_3 units are composed of two P_2 dumbbells and three Se atoms. The P_4Se_4 polymers are attached to Cu atoms, which are exclusively connected with the bridge-head P atoms. The Cu forms a distorted tetrahedral coordination with two I atoms and two P atoms. The optimized lattice parameters of the bulk $(CuI)P_4Se_4$ are $a = 11.99$ Å, $b = 14.83$ Å, and $c = 12.37$ Å. The results agree well with the experimental values of $a = 12.03$ Å, $b = 14.77$ Å, and $c = 12.45$ Å [54]. Similar to most 2D monolayer materials [70–73], the corresponding 2D monolayer of $(CuI)P_4Se_4$ can be obtained from the bulk counterpart by the exfoliation. Therefore, we have verified theoretically the feasibility of micromechanical cleavage method to obtain monolayer from the bulk by calculating the cleavage energy (E_{cl}). A four-atomic-layer model system is constructed to calculate the change of cleavage energy as the cleavage distance increases. The calculated E_{cl} of 2D $(CuI)P_4Se_4$ monolayer is around 0.26 J/m^2, which is lower than those of graphene (0.31 J/m^2) and black phosphorene (0.40 J/m^2) [74,75]. Thus, it is feasible to synthesize 2D $(CuI)P_4Se_4$ monolayer from its bulk counterpart by the exfoliation method.

The structure of the $(CuI)P_4Se_4$ monolayer obtained by optimizing is shown in Fig. 1(a). Obviously, the $(CuI)P_4Se_4$ monolayer has no dangling bond and the neutral polymeric P_4Se_4 strands still links with Cu_2I_2 units, indicating that the dimensionality reduction does not affect the integrity of the $(CuI)P_4Se_4$ monolayer. The $(CuI)P_4Se_4$ monolayer belongs to *Pmna* (No. 53) space group with lattice parameters $a = 11.70$ Å and $b = 14.78$ Å. The unit cell contains four P_4Se_4 and two Cu_2I_2 units. The P_4Se_4 strands spread along the *y* direction. The Cu-Cu bonds of the Cu_2I_2 units linked with the four bridge-head P atoms are also along the *y* direction.

To verify the stability of the $(CuI)P_4Se_4$ monolayer at room temperature, we calculated the phonon spectrum and performed the AIMD simulation. The calculated phonon spectrum is shown in Fig. 1(b). It can be found that the largest frequency reaches to 12.76 THz. At the same time, the phonon spectrum of the $(CuI)P_4Se_4$ monolayer only has a negligible imaginary frequency at the high-symmetric Γ point in the whole Brillouin zone, which indicates that it has dynamic stability. At the same time, the AIMD simulation was carried out at 300 K for 10 ps with a time step of 2 fs, and the results were shown in Fig. 1(c). The total energy of the $(CuI)P_4Se_4$ monolayer fluctuates around the equilibrium value. After the simulation, the 2D structure of the $(CuI)P_4Se_4$ monolayer maintains well. Although there is a slight structure deformation, no obvious bond breaking occurs. This proves that the $(CuI)P_4Se_4$ monolayer exhibits good thermal stability. The stability of $(CuI)P_4Se_4$ monolayer at room temperature is the essential precondition for practical device applications.

B. Electronic and optical properties

As shown in Fig. 1(d), the projected band structure of $(CuI)P_4Se_4$ monolayer is calculated by the HSE06 functional. It can be found that the $(CuI)P_4Se_4$ monolayer is an indirect semiconductor with a band gap of 2.66 eV. The conduction band minimum (CBM) and valence band maximum (VBM)

are located at the Γ and S points, respectively. However, the direct band gap at the Γ point is 2.67 eV, which is very close to the indirect band gap. Thus, the (CuI)P_4Se_4 monolayer can be considered as a quasidirect semiconductor material. The band edge of valence band exhibits a typical Mexican-hat-like dispersion around the S point, leading to a sharp density of states (DOS). This so-called van Hove singularity point could induce electronic instability, which is conducive to the acquisition of ferromagnetism by hole doping. From projected band structure and partial density of states (PDOS) shown in Fig. 1(d), it is clear that the CBM is mainly composed of the p orbitals of P and Se atoms, while the VBM is mainly occupied by the d orbitals of Cu atoms and p orbitals of I atoms. Obviously, the P_4Se_4 strands and Cu_2I_2 units dominate the state distributions around the CBM and VBM, respectively. This is in good agreement with the electron density distributions in Fig. 1(e). Furthermore, the optical absorption of the (CuI)P_4Se_4 monolayer was examined based on HSE06 functional. As shown in the Fig. 1(f), the (CuI)P_4Se_4 monolayer has anisotropic optical absorption capacity and the optical absorption in the y direction is greater than that in the x direction. In addition, the optical absorption of (CuI)P_4Se_4 monolayer begins from the visible regions and is mainly concentrated in the ultraviolet light region.

C. Mechanical properties

Unusual structures often produce special mechanical properties. Second-order elastic constants play a pivotal role in shaping the mechanical and dynamical characteristics of materials, with a particular emphasis on stability and stiffness [76,77]. In the linear elastic range, the stress response of solids to external loading strain adheres to the generalized Hooke's law and can be expressed more concisely using Voigt notation [78]:

$$\sigma_i = \sum_{j=1}^{6} C_{ij}\varepsilon_j, \tag{1}$$

where σ_i and ε_j represent the stress and strain vectors, respectively. The subscripts i and j for the components of σ_i and ε_j can be indicated as $1 = xx$, $2 = yy$, $3 = zz$, $4 = yz$, $5 = zx$, and $6 = xy$. The elastic stiffness tensor, denoted as C_{ij}, can be obtained by evaluating the first-order derivative of the stress-strain curves based on Eq. (1) [79,80], named as stress vs strain method. Besides, an alternative theoretical method for calculating elastic constants involves assessing the energy variation through the application of minor strains to the equilibrium lattice configuration [81]. For 2D materials, only in-plane 1 (xx), 2 (yy), and 6 (xy) components for strain ε and stress tensors σ are considered. Thus, the elastic strain energy per unit area can be expressed as [82,83]

$$U(\varepsilon) = \tfrac{1}{2}C_{11}\varepsilon_{xx}^2 + \tfrac{1}{2}C_{22}\varepsilon_{yy}^2 + C_{12}\varepsilon_{xx}\varepsilon_{yy} + 2C_{66}\varepsilon_{xy}^2, \tag{2}$$

where C_{11}, C_{12}, C_{22}, and C_{66} are the linear elastic constants of 2D systems, representing the second-order derivatives of strain energy with respect to strain. These elastic constants are obtained by fitting energy curves associated with both uniaxial and equibiaxial strains based on Eq. (2). This method is commonly referred to as energy vs strain method. In the calculations for 2D (CuI)P_4Se_4 monolayer, the corresponding strain is chosen in the range of −0.02 to 0.02 with increments of 0.005. The linear elastic constants (C_{ij}) can be derived through postprocessing the data obtained from VASP calculations by using the VASPKIT code [65]. The corresponding results are summarized in Table I. Based on the energy vs strain (stress vs strain) method, the elastic constants are calculated to be $C_{11} = 8.62$ (8.17) N/m, $C_{12} = 0.16$ (0.35) N/m, $C_{22} = 41.81$ (41.23) N/m, and $C_{66} = 3.78$ (3.96) N/m for the (CuI)P_4Se_4 monolayer. Note that the two calculation methods can yield similar results. Obviously, the elastic constants satisfy the Born criterion of C_{11}, C_{22}, $C_{66} > 0$ and $C_{11}C_{22} - C_{12}^2 > 0$, indicating that 2D (CuI)P_4Se_4 monolayer has good mechanical stability. In addition, the relatively small elastic constants may endow (CuI)P_4Se_4 monolayer with good mechanical flexibility.

TABLE I. The elastic constants of the (CuI)P_4Se_4 monolayer calculated by using both the energy vs strain and stress vs strain methods.

Method	C_{11} (N/m)	C_{12} (N/m)	C_{22} (N/m)	C_{66} (N/m)
Energy vs strain	8.62	0.16	41.81	3.78
Stress vs strain	8.17	0.35	41.23	3.96

The (CuI)P_4Se_4 monolayer crystalizes in the *Pmna* (No. 53) space group, which belongs to the orthorhombic symmetry. The Young's modulus $Y(\theta)$ and Poisson's ratio $\upsilon(\theta)$ along the in plane θ for the 2D materials with the orthorhombic symmetry can be obtained from the elastic constants by the following formula [84]:

$$Y(\theta) = \frac{C_{11}C_{22} - C_{12}^2}{C_{11}\sin^4\theta + A\sin^2\theta\cos^2\theta + C_{22}\cos^4\theta}, \tag{3}$$

$$\upsilon(\theta) = \frac{C_{12}\sin^4\theta - B\sin^2\theta\cos^2\theta + C_{12}\cos^4\theta}{C_{11}\sin^4\theta + A\sin^2\theta\cos^2\theta + C_{22}\cos^4\theta}, \tag{4}$$

where $A = \frac{C_{11}C_{22}-C_{12}^2}{C_{66}} - 2C_{12}$ and $B = C_{11} + C_{22} - \frac{C_{11}C_{22}-C_{12}^2}{C_{66}}$. Here, the elastic constants calculated by the energy vs strain method are used to evaluate the $Y(\theta)$ and $\upsilon(\theta)$ of (CuI)P_4Se_4 monolayer. The $Y(\theta)$ is shown in Fig. 2(a). The maximum value of $Y(\theta)$ is 41.81 N/m along the y direction (at $\theta = 90°$ and 270°), while the minimum value is 8.47 N/m at $\theta = 21°$, 159°, 201°, and 339°. In particular, the $Y(\theta)$ in the x direction is 8.62 N/m (at $\theta = 0°$ and 180°), also obviously smaller than that in the y direction. The difference of $Y(\theta)$ in the whole 2D plane indicates that the (CuI)P_4Se_4 monolayer has strong mechanical anisotropy, which is caused by the anisotropic geometrical structure. At the same time, the $Y(\theta)$ of (CuI)P_4Se_4 monolayer is much smaller than those of previously reported 2D materials, such as h-BN (275.8 N/m) [78], B_4N (268 N/m) [48], and MoS_2 (123 N/m) [85], indicating the excellent mechanical flexibility of (CuI)P_4Se_4 monolayer.

As shown in Fig. 2(b), the Poisson's ratio $\upsilon(\theta)$ of (CuI)P_4Se_4 monolayer also exhibits obvious anisotropy and spatial variability. Of particular importance, the (CuI)P_4Se_4 monolayer shows fascinating near ZPR phenomena along both the x and y directions. The υ along the x and y directions can be calculated by the formula $\upsilon_x = \frac{C_{21}}{C_{22}}$ and $\upsilon_y = \frac{C_{12}}{C_{11}}$.

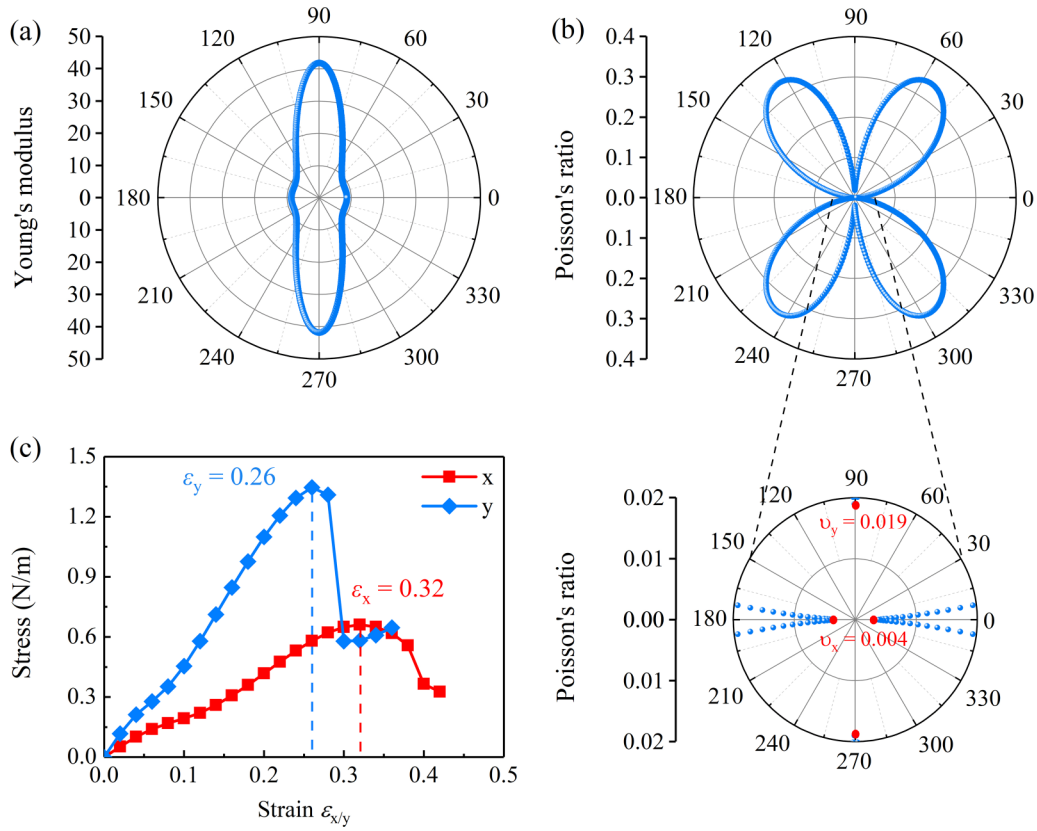

FIG. 2. (a) The Young's modulus and (b) Poisson's ratio of the $(CuI)P_4Se_4$ monolayer as functions of the in-plane angle θ. $\theta = 0°$ corresponds to the x direction. (c) The calculated stress-strain relations of the $(CuI)P_4Se_4$ monolayer under the tensile strain along the x (0°) and y (90°) directions.

Since C_{12} and C_{21} are much smaller than C_{11} and C_{22}, the calculated υ_x and υ_y of $(CuI)P_4Se_4$ monolayer are close to 0, e.g., 0.004 and 0.019, respectively. Such small values of υ can be regarded as near NPR, especially for υ_x. This means that 2D $(CuI)P_4Se_4$ monolayer does not transversally deform in response to an axial strain along the x direction. At the same time, the transversal deformation is very small with respect to an axial strain along the y direction. In addition, the $(CuI)P_4Se_4$ monolayer still has a normal PPR along other in-plane directions, where it reaches a maximum of 0.34 at $\theta = 56°, 124°, 236°$, and 304°.

To further investigate the mechanical properties of $(CuI)P_4Se_4$ monolayer, the ideal strength of the material is examined by calculating the stress-strain curves. The relationship between stress and tensile strain in the x and y directions is shown in Fig. 2(c). The $(CuI)P_4Se_4$ monolayer has a linear stress-strain relationship under very small strains. With the increase of strain, the linear relation of stress-strain curve vanishes, while the elastic anisotropy is notable. The critical tensile strains of 2D $(CuI)P_4Se_4$ monolayer in the x and y directions are 0.32 and 0.26, respectively, which is larger than MoS_2 (0.06 ∼ 0.11 and 0.23) [85], W_4PCl_{11} (0.13 and 0.15) [71], B_4N (0.19 and 0.18) [48], and graphene (0.19 and 0.27) [78], and comparable to InSeBr (0.21 and 0.33) [86] and phosphorene (0.27 and 0.30) [39,40]. In addition, as an important mechanical property of material, the ideal strength is the maximum stress that a material can withstand under the critical condition of plastic deformation. As shown in Fig. 2(c), the critical stresses in the x and y directions are 0.66 and 1.35 N/m, respectively. The ideal strengths are much less than those of most reported 2D materials, such as graphene (34 N/m) [78], B_4N (11 and 25 N/m) [48], black phosphorus (16 N/m) [50], MoS_2 (15 N/m) [85], phosphorene (4 and 10 N/m) [39], and InSeBr (4.94 and 4.72 N/m) [86]. Noteworthy, the microideal strength corresponds to the small Young's modulus, indicating that $(CuI)P_4Se_4$ monolayer is a 2D material with ultrastrong flexibility, which is expected to be applied in the field of high flexibility requirement.

D. Strain-dependent near ZPR and NPR

In-plane uniaxial strain ranging from −0.12 to 0.12 is applied in the x and y directions, respectively, to explore the anisotropic Poisson's ratio of $(CuI)P_4Se_4$ monolayer. The responses of 2D $(CuI)P_4Se_4$ monolayer with respect to in-plane uniaxial strain are shown in Fig. 3. The strain is defined as $\varepsilon = \frac{l-l_0}{l_0}$, where $\varepsilon = \varepsilon_x$ and ε_y represent the relative strain along the x and y directions, respectively; $l = a$, b, and h represent the lattice constants along the x and y directions and thickness of layer under the applied strain, respectively; and $l_0 = a_0$, b_0, and h_0 are the lattice constants and thickness of layer without the applied strain, respectively. The Poisson's ratio can be defined as $\upsilon = -\frac{\partial\varepsilon_1}{\partial\varepsilon_2}$, where ε_1 is response strain driven by forced strain ε_2. As shown in Fig. 3(a), the total energy variations of $(CuI)P_4Se_4$ monolayer seem to be a

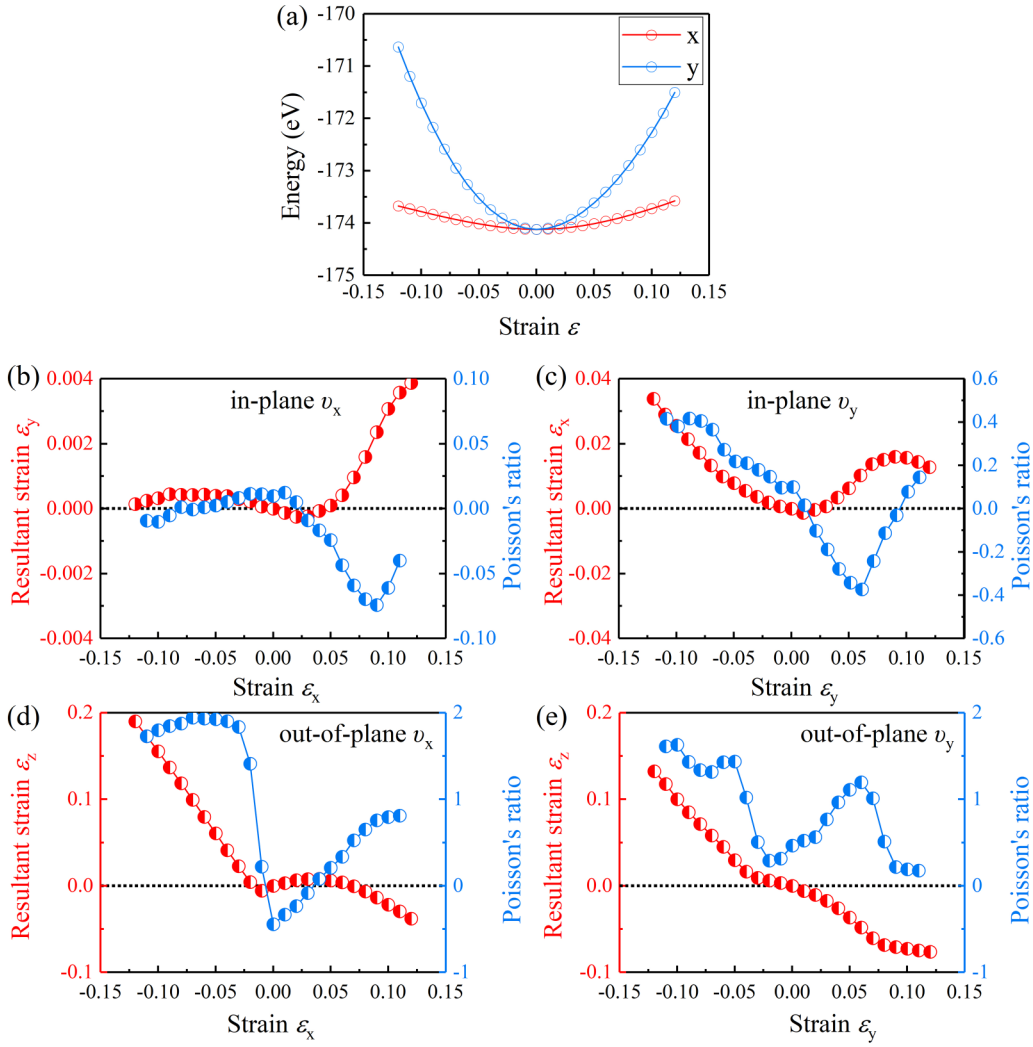

FIG. 3. (a) The energy variations of the $(CuI)P_4Se_4$ monolayer under the uniaxial strain along the x and y directions. The in-plane mechanical responses of the $(CuI)P_4Se_4$ monolayer under uniaxial strain along the (b) x and (c) y directions, respectively. The out-of-plane mechanical responses of the $(CuI)P_4Se_4$ monolayer under the uniaxial strain along the (d) x and (e) y directions, respectively.

parabola when the strains is applied, indicating the complete optimization of unstrained structure.

The in-plane Poisson's ratios υ_x and υ_y are first studied. As shown in Fig. 3(b), when the strain ε_x is applied in the x direction in a relatively large range of -0.12 to 0.03, the variation of resultant strain ε_y along the y direction is very small and the calculated in-plane Poisson's ratio υ_x is within ± 0.01, indicating the near ZPR characteristic in the x direction. When the tensile strain ε_x is enlarged to the range of 0.04 to 0.12, the $(CuI)P_4Se_4$ monolayer then exhibits NPR behavior, showing the increase of resultant strain ε_y with the increase of ε_x. The maximal value of NPR is -0.074 at $\varepsilon_x = 0.09$. The transition between near ZPR and NPR under strain may be useful for special function applications of $(CuI)P_4Se_4$ monolayer.

It is worth noting that ZPR behavior is not found when strain is applied in the y direction. As shown in Fig. 3(c), the $(CuI)P_4Se_4$ monolayer exhibits PPR behavior under compressive strain ε_y along the y direction. The lattice a will be expanded gradually with the enhancement of compressive strain ε_y. When the tensile strain ε_y (>0.01) is applied, the transition from PPR to NPR has happened. The NPR ranges from $\varepsilon_y = 0.02$ to 0.09 and the maximal value of NPR is -0.37 at $\varepsilon_y = 0.06$. Once the ε_y exceeds 0.10, the υ_y becomes positive again. This strain-dependent transition between PPR and NPR has also been proposed in 2D materials [5,8]. The significant difference about Poisson's ratio in the response to uniaxial strain in the x and y directions proves that the 2D $(CuI)P_4Se_4$ material has strong in-plane mechanical anisotropy.

In addition, the out-of-plane Poisson's ratios υ_x and υ_y were also studied. As shown in Fig. 3(d), when the compressive strain is applied in the x direction, the $(CuI)P_4Se_4$ monolayer exhibits PPR behavior with a maximum PPR of 1.944. When the strain is converted from compressive one into tensile one, the $(CuI)P_4Se_4$ monolayer may exhibit NPR behavior in a small range of $\varepsilon_x = 0$ to 0.04 with a maximum NPR of -0.44. At this moment the thickness of layer h will increase slightly with the increase of tensile strain ε_x. However, when the ε_x is larger than 0.04, this NPR characteristic and out-of-plane auxetic effect will vanish. The thickness of layer h starts to decrease in large tensile strain. This strain-dependent out-of-plane Poisson's ratio may also originate

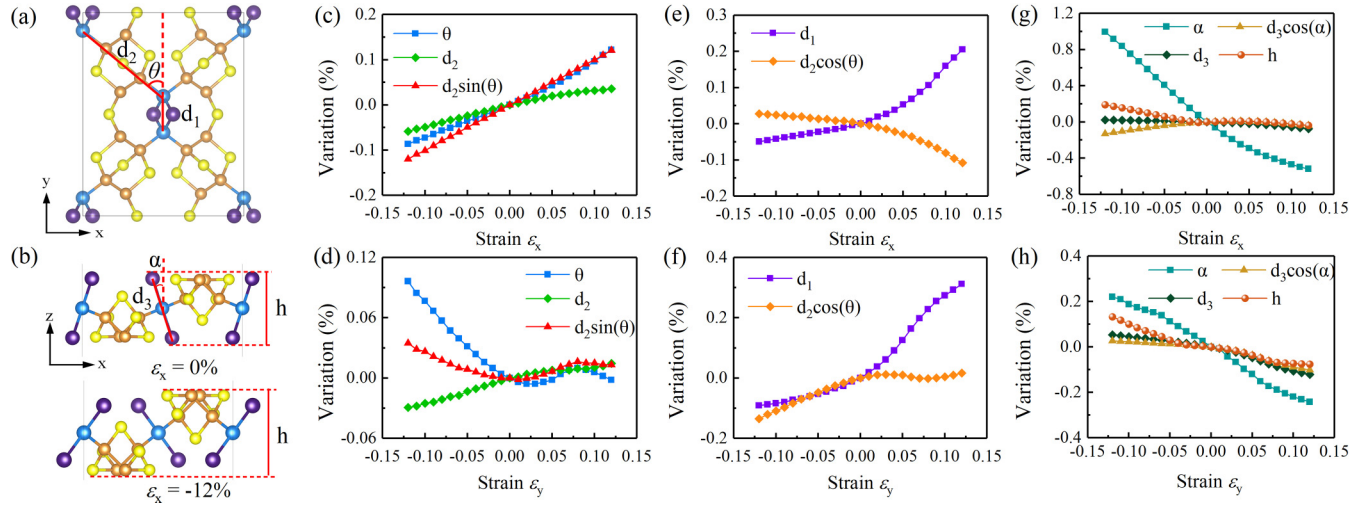

FIG. 4. The definition of (a) in-plane and (b) out-of-plane geometrical parameters of the (CuI)P_4Se_4 monolayer: distances d_1 and d_2 and angle θ; distance d_3, thickness of layer h, and angle α. The evolution of the key geometrical parameters with respect to the applied strains along the (c), (e), and (g) x and (d), (f), and (h) y directions, respectively. The $d_2\sin(\theta)$ and $d_2\cos(\theta)$ are the projection lengths of the distance d_2 along the x and y directions, respectively. The $d_3\cos(\alpha)$ is the projection length of the distance d_3 along the z direction.

from the special geometrical and electronic properties. As shown in Fig. 3(e), the (CuI)P_4Se_4 monolayer only exhibits out-of-plane PPR behavior when the strain is applied along the y direction. The maximum PPR of 1.63 is at $\varepsilon_y = -0.1$. The different out-of-plane Poisson's ratio behaviors under the uniaxial strain along the x and y directions further confirm the strong mechanical anisotropy in the (CuI)P_4Se_4 monolayer.

E. Mechanistic explanation of near ZPR and NPR

To find the origin of in-plane strain-dependent near ZPR and NPR in the (CuI)P_4Se_4 monolayer, we consider the change of key geometric parameters, such as in-plane atomic distances and angles, under the uniaxial strain. This method has also been used for discussing the NPR behavior in some 2D honeycomb structures [5]. As shown in Fig. 4(a), we defined two atomic distances d_1 and d_2 and one atomic angle θ. d_1 and d_2 represent nearest-neighbor and next-nearest-neighbor distances between two Cu atoms in the unit cell. θ represents the angle between d_1 and d_2. Then the relationship of lattice constants a and b with d_1, d_2, and θ can be expressed as

$$a = 2d_2\sin(\theta), \tag{5}$$

$$b = 2[d_1 + d_2\cos(\theta)]. \tag{6}$$

It is obvious that the lattice constant a is controlled by angle θ and distance d_2, while the lattice constant b is controlled by angle θ and distances d_1 and d_2. Therefore, we calculated the variations of d_1, d_2, and θ under in-plane uniaxial strains ranging from -0.12 to 0.12. The results are summarized in Figs. 4(c)–4(f).

It is not hard to understand that θ and d_2 can increase (decrease) gradually with the increase of tensile (compressive) strain along the x direction [see Fig. 4(c)], resulting in a continuous increase of $d_2\sin(\theta)$ from $\varepsilon_x = -0.12$ to 0.12. As shown in Fig. 4(e), the variation trend of projection length $d_2\cos(\theta)$ is opposite to that of distances d_1 in the whole strain range. Based on Eq. (6), the lattice constant b is dominated by $d_2\cos(\theta)$ and d_1. For the compressive and small tensile strain ($\varepsilon_x = -0.12 \sim 0.03$), the decreasing rate of $d_2\cos(\theta)$ is very close to the increasing rate of d_1 and their contributions to lattice constant b may cancel each other out. This leads to very small variations of resultant strain ε_y and in-plane Poisson's ratio υ_x, showing the near ZPR behavior along the x direction in Fig. 3(b). However, for the large tensile strain ($\varepsilon_x = 0.04 \sim 0.12$), the increasing rate of d_1 is obviously greater than the decreasing rate of $d_2\cos(\theta)$, inducing the increase of the resultant strain ε_y and the NPR characteristic along the x direction in Fig. 3(b).

The lattice constant b is continuously enlarged and reduced to simulate the uniaxial tensile and compressive strains ε_y along the y direction. The corresponding variations of in-plane θ, d_1, d_2, $d_2\cos(\theta)$, and $d_2\sin(\theta)$ are also explored and summarized in Figs. 4(d) and 4(f). The values of d_1 and d_2 normally decrease (increase) with increasing of the compressive (tensile) strains. On the other hand, the value of θ obviously increases with increasing of the compressive strains, but the trend with respect to tensile strains is relatively complex. θ first go down in small tensile strains, and then rises under a certain range, and finally, it is on the decrease again. Based on Eq. (5), the lattice constant a is dominated by the value of $d_2\sin(\theta)$. Obviously, the variation of $d_2\sin(\theta)$ in Fig. 4(d) is in good agreement with the trend of resultant strain ε_x under the strain ε_y condition in Fig. 3(c). Therefore, the main influential factor of in-plane Poisson's ratio υ_y is the angle θ. Strain ε_y promotes the variations of θ and $d_2\sin(\theta)$, inducing the transition between in-plane PPR and NPR along the y direction.

The (CuI)P_4Se_4 monolayer possesses special 2D structure, composed of P_4Se_4 strands and Cu_2I_2 units. The P_4Se_4 strands mainly support the structure response with respect to the different strains. This leads to the strain-dependent in-plane NPR and near ZPR in 2D (CuI)P_4Se_4 monolayer. From the above mechanistic explanation, we find that the appearance of NPR along the x direction is due to the unusual increase of distance

d_1 and the in-plane NPR along the y direction is mainly caused by the sudden increase of angle θ. Such variations of distance and angle can be attributed to the complicated structure response with respect to strains.

For out-of-plane Poisson's ratio, we also defined two critical quantities, angle α and distance d_3, which determine the thickness of layer h of (CuI)P_4Se_4 monolayer. As shown in Fig. 4(b), the α represents the angle of inclination relative to vertical direction of Cu_2I_2 units and d_3 is the distance between the two I atoms in one Cu_2I_2 unit. When the thickness of the (CuI)P_4Se_4 monolayer is dominated by the Cu_2I_2 units, the relationship of thickness of layer h with d_3 and α can be expressed as

$$h = d_3\cos(\alpha). \tag{7}$$

It is clear that h is controlled by the values of α and d_3. Therefore, we also calculated the variations of d_3 and α under in-plane uniaxial strains ranging from -0.12 to 0.12. Figures 4(g) and 4(h) summarize the results for the applied strains along the x and y directions, respectively.

When the tensile strain is applied along the x direction, the Cu_2I_2 units determine the thickness and Eq. (7) is absolutely tenable, inducing that h agrees well $d_3\cos(\alpha)$ in Fig. 4(g). Due to the special geometrical structure of the (CuI)P_4Se_4 monolayer, the plane of Cu_2I_2 units may rotate by the effect of resultant moment under the condition of the tensile strain in the x direction. This results in that the angle α decreases sharply with the increase tensile strain in the range of $\varepsilon_x = 0 \sim 0.04$. In this process, the decrease of d_3 is relatively slow [see Fig. 4(g)]. Because the decreasing rate of α is obviously greater than the decreasing rate of d_3 in the small strain, an increasing trend has begun in $d_3\cos(\alpha)$, representing the thickness of layer h. This indicates that the (CuI)P_4Se_4 monolayer possesses the out-of-plane NPR characteristic under the condition of applying small tensile strain along the x direction. If the tensile strain continues to increase along the x direction, e.g., >0.05, the decreasing trend of α is slowed obviously in Fig. 4(g), leading to the decrease of $d_3\cos(\alpha)$ and h. At this point, the out-of-plane NPR behavior has turned into the normal PPR one. On the other hand, when the compressive strain is applied along the x direction, the angle α increases sharply with the increase of strain. However, the strong structure distortion may lead to the obvious bulge of the P_4Se_4 strands along the z direction [see Fig. 4(b)]. Meanwhile, the thickness of layer h is naturally dominated by the P_4Se_4 strands and Eq. (7) is completely invalid. Thus, the normal out-of-plane PPR behavior has been found under the condition of compressive strain along the x direction.

As shown in Fig. 4(h), when the strain is applied in the y direction, the angle α decreases (increases) relatively slowly with the increase of tensile (compressive) strain. Although the thickness of layer h is also dominated by the Cu_2I_2 units in small tensile and compressive strains, the variation of $d_3\cos(\alpha)$ only induces the normal PPR. Moreover, under large tensile or compressive strains, h becomes to be dominated by P_4Se_4 strands. However, this does not affect the out-of-plane PPR behavior of (CuI)P_4Se_4 monolayer in the y direction.

F. Further understanding from electronic response

It can be seen that the in-plane Poisson's ratio possesses obvious strain-dependent characteristics, showing the transformation between PPR and NPR and near ZPR under different in-plane strains. The variations of atomic distances d_1 and d_2 and angle θ with respect to strains are very interesting but anomalous. Thus, we also use the electronic properties and geometric response approaches to gain insight into the counterintuitive behavior in (CuI)P_4Se_4 monolayer. Figures 5(a) and 5(b) depict the ELF of the (CuI)P_4Se_4 monolayer. The ELF contains information about the probability of electron pair, but also the patterns of bonding can be observed. In (CuI)P_4Se_4 monolayer, the norbornane analogous P_4Se_3 units are linked by the bridging Se atoms to form P_4Se_4 strands. At the same time, the bridging Se atoms are located on either side of Cu_2I_2 units. As shown in Figs. 5(a) and 5(b), it can be found that the P_4Se_4 strands are covered with electron clouds, indicating that the P_4Se_4 strands are linked through covalent bonds. The two I atoms in Cu_2I_2 units have hypertrophic electron clouds, while the two Cu atoms have no electron clouds. Thus, Cu atoms mainly lose electrons and form ionic bonds with the I and P atoms. The different bond characteristics between the P_4Se_4 and Cu_2I_2 units may cause the different variation trend of distances d_1 and d_2 and angle θ under the strain conditions.

Figure 5(c) shows the geometric response of (CuI)P_4Se_4 monolayer under the condition of tensile strain applied in the x direction. The Cu atoms are subjected to the stretching force along the x direction (red arrows). This tensile force can be divided into two parts: The forces along atomic distance d_2 (green arrows) and perpendicular to d_2 (blue arrows). It can be found that the forces represented by the green arrows affect the increase in atomic distance d_2, resulting in the in-plane NPR, while the forces represented by the blue arrows promote the increase in angle θ, resulting in the in-plane PPR. Moreover, the two Cu atoms in one Cu_2I_2 unit are subject to the upward and downward resultant forces (purple arrows), respectively, leading to the increase of atomic distance d_1, which determines the in-plane NPR in Fig. 3(b).

Moreover, the tensile strain along the y direction can also induce the presence of the NPR. The geometric response of (CuI)P_4Se_4 monolayer under the tensile strain along the y direction is also analyzed and displayed in Fig. 5(d). For applying the y-direction tensile strain, the Cu atoms and outermost Se atoms are subjected to the stretching force (red arrow) along the y direction. Such stretching force can also be divided into two components that are along the d_2 direction (green arrow) and perpendicular to the d_2 direction (blue arrow). It is clear that the force represented by the green arrow will affect the increase of atomic distance d_2, resulting in the in-plane NPR, while the force represented by the blue arrow will promote the decrease of angle θ, resulting in the in-plane PPR. In addition, the Cu atoms continue to experience upward and downward resultant forces, which leads to the increase in the atomic distance d_1. Therefore, the variation of in-plane Poisson's ratio υ_y mainly depends on the competition between the atomic distances d_1 and d_2 and angle θ. As shown in Fig. 4(d), the in-plane NPR behavior in the y direction is due to the sudden increase in the angle θ under small tensile strain.

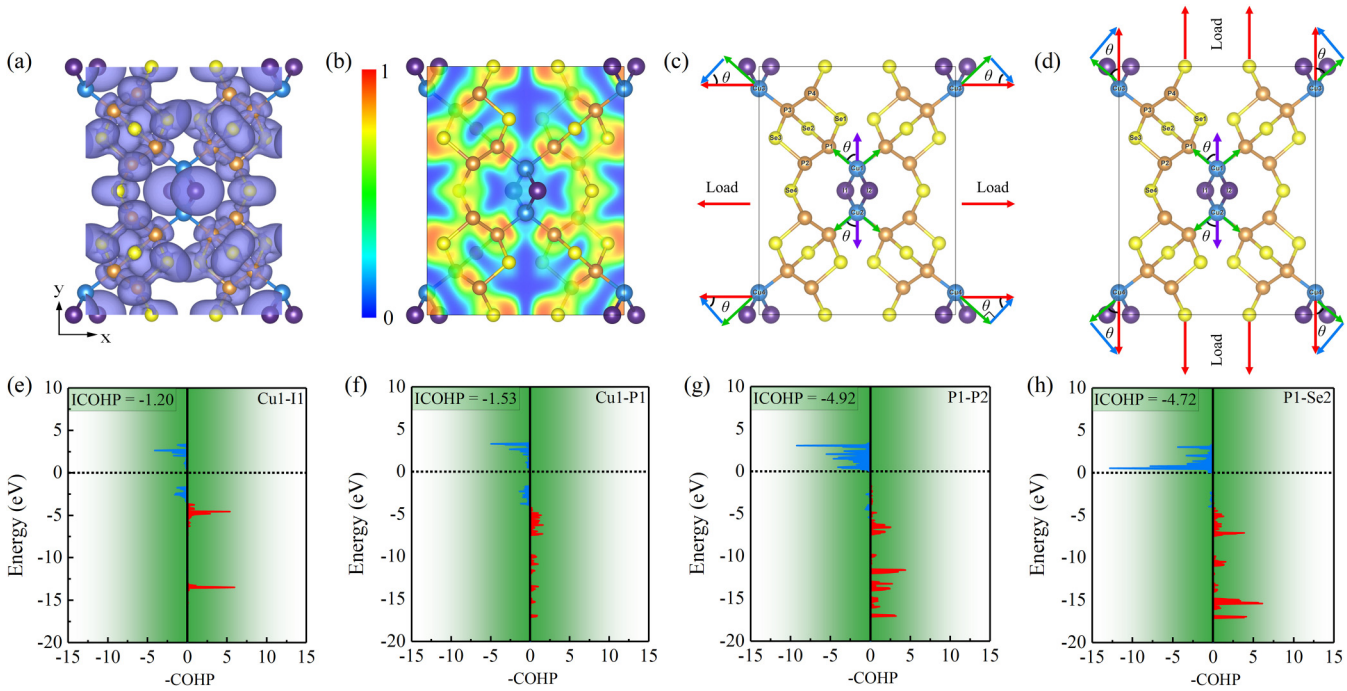

FIG. 5. The (a) 3D and (b) 2D electron localization function (ELF) of the $(CuI)P_4Se_4$ monolayer. The geometric responses of the $(CuI)P_4Se_4$ monolayer under the uniaxial tensile strains along the (c) x and (d) y directions, respectively. Negative of crystal orbital Hamilton population (−COHP) of the local (e) Cu–I, (f) Cu–P, (g) P–P, and (h) P–Se bonds in the $(CuI)P_4Se_4$ monolayer. The integrated COHP (ICOHP) of these bonds are also shown. The dashed line indicates the Fermi level.

To further investigate the origin of NPR in the y direction, we used the COHP method to study the differences between ionic and covalent bonds in the $(CuI)P_4Se_4$ monolayer. As shown in Figs. 5(e)–5(h), it can be found that the ionic bonds formed by Cu-I and Cu-P have relatively more antibonding states below the Fermi level, while the covalent bonds formed by P-P and P-Se have fewer antibonding states below the Fermi level. The integrated COHP (ICOHP) of each bond is obtained by integrating up to the Fermi level of COHP values. The ICOHP of covalent bonds is much greater than the ICOHP of ionic bonds, indicating that the covalent bonds of P-P and P-Se in the P_4Se_4 strands are stronger than ionic bonds of Cu-I and Cu-Se in the Cu_2I_2 units. Therefore, the P_4Se_4 strands along the y direction are not easily elongated when the tensile strain is applied. It means that the increase rate of d_2 is relatively small under the tensile strain. However, the Cu_2I_2 units dominated by weak ionic bonds are more easily stretched by y-direction tensile strain, leading to the large increase rate of d_1. The difference of variation rates between d_1 and d_2 is directly responsible to the sudden increase of angle θ under a certain range of tensile strain in Fig. 4(d). To sum up, the strain-response capabilities of P_4Se_4 and Cu_2I_2 units are crucial to the in-plane NPR behavior in the $(CuI)P_4Se_4$ monolayer.

G. Strain-dependent electronic properties

It is well known that strain engineering can regulate the electronic properties of materials. The strain in low-dimensional materials can be introduced by the substrate or external environment. Therefore, we also studied the electronic properties of the $(CuI)P_4Se_4$ monolayer under the uniaxial strains at the HSE06 level. Figure 6 shows that the evolutions of band-edge positions and band gap of the $(CuI)P_4Se_4$ monolayer under the uniaxial strain range from −0.06 to 0.06 along the x and y directions. As shown in Fig. 6(a), when the strain is applied in the x direction, the band gap increases slightly from 2.66 to 2.74 eV with the increase of tensile strain and also decreases slightly from 2.66 to 2.55 eV with the increase of compressive strain. At the same time, the CBM is always located at the Γ point under the strain ε_x ranging from −0.06 to 0.04. Once the strain is larger than 0.06, the location of CBM will move to the S point, leading to the direct-band-gap characteristic. Although the VBM is always located at the S point, the energy difference of the band edges between the Γ and S points is very small. Therefore, the $(CuI)P_4Se_4$ monolayer remains a quasidirect-band-gap semiconductor in the strain range of −0.06 to 0.04.

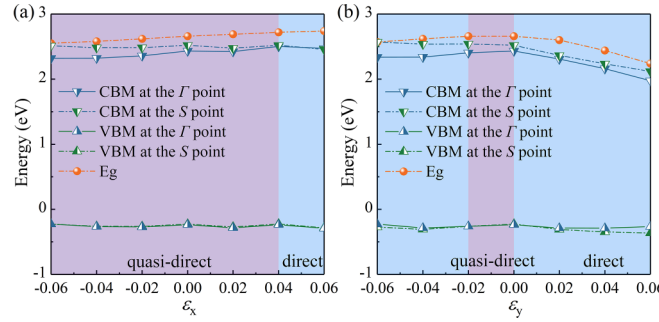

FIG. 6. The band-edge positions and band gap of 2D $(CuI)P_4Se_4$ monolayer under the uniaxial strain range from −0.06 to 0.06 along the (a) x and (b) y directions, respectively. The Fermi level is set at zero.

When the strain is applied in the y direction, the band gap fleetly decreases with the increase of tensile strain (e.g., 2.24 eV at $\varepsilon_y = 0.06$) and sightly decreases with the increase of compressive strain (e.g., 2.57 eV at $\varepsilon_y = -0.06$). Moreover, the CBM is always located at the Γ point, and the energy difference of band edges between the Γ and S points is relatively large. The VBM is basically always at the Γ point, only at the S point when the strains are -0.02 and 0, determining that the transform between quasidirect and direct band gap is more likely to occur under the y-direction strain. The different responses of the electronic properties under the strain applied along the x and y directions indicate the obvious anisotropy of the $(CuI)P_4Se_4$ monolayer. Finally, the conversion 2D $(CuI)P_4Se_4$ monolayer from indirect to direct semiconductor under strain may be also beneficial for applications in optoelectronics and eletromechanics.

IV. CONCLUSIONS

In summary, we theoretically predict a potential 2D auxetic $(CuI)P_4Se_4$ monolayer based on the first-principles calculations. The $(CuI)P_4Se_4$ monolayer can be obtained from its bulk counterpart by exfoliation methods. It is a quasidirect-band-gap semiconductor with a relatively large band gap of 2.66 eV, which can be regulated by applying the uniaxial strains. In particular, the unusual 2D structure endows the $(CuI)P_4Se_4$ monolayer with special mechanical properties, such as much smaller ideal tensile strength, excellent flexibility, and obvious mechanical anisotropy. Very importantly, the Poisson's ratio calculations indicate that the $(CuI)P_4Se_4$ monolayer possesses strain-dependent near ZPR and NPR characteristics. Further analyses show that the distances and angles between the neighbor Cu atoms are the primary determinants of the transition between PPR and NPR behaviors under the in-plane uniaxial strains. In addition, the electronic and geometric responses under the strains determine that the NPR behavior in the $(CuI)P_4Se_4$ monolayer is mainly triggered by the difference of strain-response capabilities between the P_4Se_4 and Cu_2I_2 units. This is confirmed by the calculations of bonding type and strength in the adduct. Our work shows that 2D $(CuI)P_4Se_4$ monolayer provides a promising platform to understand the strain-dependent mechanical flexibility and extends the family of 2D near ZPR and NPR materials. Significantly, research on 2D auxetic materials is still in its early stages, with a significant number of studies often confined to the theoretical prediction phase. This indicates that 2D auxetic materials may face several challenges and open questions in the process of practical applications, such as the synthesis and preparation of high-quality and large-area 2D auxetic materials, deeper understanding of the structure-property relationships, and comprehending the size effects of auxetic characteristics. Therefore, the strain-dependent near ZPR and NPR properties exhibited by 2D auxetic $(CuI)P_4Se_4$ monolayer in this study warrant additional practical applications and experimental validations.

ACKNOWLEDGMENTS

This work was supported by the National Natural Science Foundation of China (Grant No. 21603056), the Natural Science Foundation of Henan Province (Grant No. 232300421216), the Key Scientific Research Project of Colleges and Universities in Henan Province (Grant No. 23A140015), and the Young Talents Program of Henan University.

[1] R. H. Baughman, J. M. Shacklette, A. A. Zakhidov, and S. Stafström, Negative Poisson's ratios as a common feature of cubic metals, Nature (London) **392**, 362 (1998).

[2] K. E. Evans, M. A. Nkansah, I. J. Hutchinson, and S. C. Rogers, Molecular network design, Nature (London) **353**, 124 (1991).

[3] M. Schenk and S. D. Guest, Geometry of Miura-folded metamaterials, Proc. Natl. Acad. Sci. USA **110**, 3276 (2013).

[4] L. Yu, Q. Yan, and A. Ruzsinszky, Negative Poisson's ratio in 1T-type crystalline two-dimensional transition metal dichalcogenides, Nat. Commun. **8**, 15224 (2017).

[5] Z. Qin, G. Qin, and M. Hu, Origin of anisotropic negative Poisson's ratio in graphene, Nanoscale **10**, 10365 (2018).

[6] J.-W. Jiang, S. Y. Kim, and H. S. Park, Auxetic nanomaterials: Recent progress and future development, Appl. Phys. Rev. **3**, 041101 (2016).

[7] J. Dagdelen, J. Montoya, M. de Jong, and K. Persson, Computational prediction of new auxetic materials, Nat. Commun. **8**, 323 (2017).

[8] Z. Zhuo, X. Wu, and J. Yang, Me-graphene: A graphene allotrope with near zero Poisson's ratio, sizeable band gap, and high carrier mobility, Nanoscale **12**, 19359 (2020).

[9] L. Yu, Y. Wang, X. Zheng, H. Wang, Z. Qin, and G. Qin, Emerging negative Poisson's ratio driven by strong intralayer interaction response in rectangular transition metal chalcogenides, Appl. Surf. Sci. **610**, 155478 (2023).

[10] V. H. Carneiro, J. Meireles, and H. Puga, Auxetic materials–A review, Mater Sci.-Pol. **31**, 561 (2013).

[11] K. E. Evans and A. Alderson, Auxetic materials: Functional materials and structures from lateral thinking! Adv. Mater. **12**, 617 (2000).

[12] C. Huang and L. Chen, Negative Poisson's ratio in modern functional materials, Adv. Mater. **28**, 8079 (2016).

[13] R. S. Lakes, Negative-Poisson's-ratio materials: Auxetic solids, Annu. Rev. Mater. Res. **47**, 63 (2017).

[14] W. Yang, Z.-M. Li, W. Shi, B.-H. Xie, and M.-B. Yang, Review on auxetic materials, J. Mater. Sci. **39**, 3269 (2004).

[15] R. Critchley, I. Corni, J. A. Wharton, F. C. Walsh, R. J. K. Wood, and K. R. Stokes, A review of the manufacture, mechanical properties and potential applications of auxetic foams, Phys. Status Solidi B **250**, 1963 (2013).

[16] J. N. Grima, L. Oliveri, D. Attard, B. Ellul, R. Gatt, G. Cicala, and G. Recca, Hexagonal honeycombs with zero Poisson's ratios and enhanced stiffness, Adv. Eng. Mater. **12**, 855 (2010).

[17] X. Gong, J. Huang, F. Scarpa, Y. Liu, and J. Leng, Zero Poisson's ratio cellular structure for two-dimensional morphing applications, Compos. Struct. **134**, 384 (2015).

[18] L. J. Gibson, K. E. Easterling, and M. F. Ashby, The structure and mechanics of cork, Proc. R. Soc. London. A: Math. Phys. Sci. **377**, 99 (1981).

[19] Y. Wu, N. Yi, L. Huang, T. Zhang, S. Fang, H. Chang, N. Li, J. Oh, J. A. Lee, M. Kozlov, A. C. Chipara, H. Terrones, P. Xiao, G. Long, Y. Huang, F. Zhang, L. Zhang, X. Lepró, C. Haines, M. D. Lima *et al.*, Three-dimensionally bonded spongy graphene material with super compressive elasticity and near-zero Poisson's ratio, Nat. Commun. **6**, 6141 (2015).

[20] H. Wang, X. Li, P. Li, and J. Yang, Ō-phosphorene: A two dimensional material with a highly negative Poisson's ratio, Nanoscale **9**, 850 (2017).

[21] A. Alderson and K. E. Evans, Rotation and dilation deformation mechanisms for auxetic behaviour in the α-cristobalite tetrahedral framework structure, Phys. Chem. Miner. **28**, 711 (2001).

[22] A. Alderson and K. E. Evans, Molecular origin of auxetic behavior in tetrahedral framework silicates, Phys. Rev. Lett. **89**, 225503 (2002).

[23] A. Alderson and K. E. Evans, Deformation mechanisms leading to auxetic behaviour in the α-cristobalite and α-quartz structures of both silica and germania, J. Phys.: Condens. Matter **21**, 025401 (2009).

[24] R. F. Almgren, An isotropic three-dimensional structure with Poisson's ratio = -1, J. Elast. **15**, 427 (1985).

[25] D. Attard and J. N. Grima, A three-dimensional rotating rigid units network exhibiting negative Poisson's ratios, Phys. Status Solidi B **249**, 1330 (2012).

[26] L. Cabras and M. Brun, Auxetic two-dimensional lattices with Poisson's ratio arbitrarily close to -1, Proc. R. Soc. A: Math. Phys. Eng. Sci. **470**, 20140538 (2014).

[27] G. Carta, M. Brun, and A. Baldi, Design of a porous material with isotropic negative Poisson's ratio, Mech. Mater. **97**, 67 (2016).

[28] L. Cabras and M. Brun, A class of auxetic three-dimensional lattices, J. Mech. Phys. Solids **91**, 56 (2016).

[29] K. E. Evans, A. Alderson, and F. R. Christian, Auxetic two-dimensional polymer networks. an example of tailoring geometry for specific mechanical properties, J. Chem. Soc. Faraday Trans. **91**, 2671 (1995).

[30] S. Balendhran, S. Walia, H. Nili, S. Sriram, and M. Bhaskaran, Elemental analogues of graphene: Silicene, germanene, stanene, and phosphorene, Small **11**, 640 (2015).

[31] G. R. Bhimanapati, Z. Lin, V. Meunier, Y. Jung, J. Cha, S. Das, D. Xiao, Y. Son, M. S. Strano, V. R. Cooper, L. Liang, S. G. Louie, E. Ringe, W. Zhou, S. S. Kim, R. R. Naik, B. G. Sumpter, H. Terrones, F. Xia, Y. Wang *et al.*, Recent advances in two-dimensional materials beyond graphene, ACS Nano **9**, 11509 (2015).

[32] K. S. Novoselov, A. K. Geim, S. V. Morozov, D.-E. Jiang, Y. Zhang, S. V. Dubonos, I. V. Grigorieva, and A. A. Firsov, Electric field effect in atomically thin carbon films, Science **306**, 666 (2004).

[33] S. Iijima and T. Ichihashi, Single-shell carbon nanotubes of 1-nm diameter, Nature (London) **363**, 603 (1993).

[34] S. Liu, H. Yin, D. J. Singh, and P.-F. Liu, Ta_4SiTe_4: A possible one-dimensional topological insulator, Phys. Rev. B **105**, 195419 (2022).

[35] S. Liu, H. Yin, and P.-F. Liu, Strain-dependent electronic and mechanical properties in one-dimensional topological insulator Nb_4SiTe_4, Phys. Rev. B **108**, 045411 (2023).

[36] F. Zhang, L. Kang, C. Liu, B. Wang, and H. Yin, The polarization-modulated electronic structure and giant tunneling-electroresistance effect of a one-dimensional ferroelectric $Ta_4OTe_9I_4$ nanowire, Appl. Phys. Lett. **123**, 202903 (2023).

[37] Y. Ma, Y. Dai, M. Guo, C. Niu, L. Yu, and B. Huang, Strain-induced magnetic transitions in half-fluorinated single layers of BN, GaN and graphene, Nanoscale **3**, 2301 (2011).

[38] Y. Ma, Y. Dai, M. Guo, and B. Huang, Graphene-diamond interface: Gap opening and electronic spin injection, Phys. Rev. B **85**, 235448 (2012).

[39] J. Dai and X. C. Zeng, Bilayer phosphorene: Effect of stacking order on bandgap and its potential applications in thin-film solar cells, J. Phys. Chem. Lett. **5**, 1289 (2014).

[40] W. Li, Y. Yang, G. Zhang, and Y.-W. Zhang, Ultrafast and directional diffusion of lithium in phosphorene for high-performance lithium-ion battery, Nano Lett. **15**, 1691 (2015).

[41] Q. H. Wang, K. Kalantar-Zadeh, A. Kis, J. N. Coleman, and M. S. Strano, Electronics and optoelectronics of two-dimensional transition metal dichalcogenides, Nat. Nanotechnol. **7**, 699 (2012).

[42] M. Chhowalla, H. S. Shin, G. Eda, L.-J. Li, K. P. Loh, and H. Zhang, The chemistry of two-dimensional layered transition metal dichalcogenide nanosheets, Nat. Chem. **5**, 263 (2013).

[43] R. Lakes, Foam structures with a negative Poisson's ratio, Science **235**, 1038 (1987).

[44] D. Prall and R. S. Lakes, Properties of a chiral honeycomb with a Poisson's ratio of -1, Int. J. Mech. Sci. **39**, 305 (1997).

[45] G. N. Greaves, A. L. Greer, R. S. Lakes, and T. Rouxel, Poisson's ratio and modern materials, Nat. Mater. **10**, 823 (2011).

[46] Y. Prawoto, Seeing auxetic materials from the mechanics point of view: A structural review on the negative Poisson's ratio, Comput. Mater. Sci. **58**, 140 (2012).

[47] R. Peng, Y. Ma, Z. He, B. Huang, L. Kou, and Y. Dai, Single-layer Ag_2S: A two-dimensional bidirectional auxetic semiconductor, Nano Lett. **19**, 1227 (2019).

[48] B. Wang, Q. Wu, Y. Zhang, L. Ma, and J. Wang, Auxetic B_4N monolayer: A promising 2D material with in-plane negative Poisson's ratio and large anisotropic mechanics, ACS Appl. Mater. Interfaces **11**, 33231 (2019).

[49] W. Jin, W. Sun, X. Kuang, C. Lu, and L. Kou, Negative Poisson ratio in two-dimensional tungsten nitride: Synergistic effect from electronic and structural properties, J. Phys. Chem. Lett. **11**, 9643 (2020).

[50] J.-W. Jiang and H. S. Park, Negative Poisson's ratio in single-layer black phosphorus, Nat. Commun. **5**, 4727 (2014).

[51] M.H. Möller and W. Jeitschko, Preparation, properties, and crystal structure of the solid electrolytes $Cu_2P_3I_2$ and $Ag_2P_3I_2$, J. Solid State Chem. **65**, 178 (1986).

[52] A. Pfitzner and E. Freudenthaler, $(CuI)_3P_{12}$: A solid containing a new polymer of phosphorus predicted by theory, Angew. Chem., Int. Ed. Engl. **34**, 1647 (1995).

[53] A. Pfitzner and E. Freudenthaler, Crystal structure of tricopper(I) pentadecaphosphide diiodide, $Cu_3P_{15}I_2$, Z. Kristallogr–Cryst. Mater. **210**, 59 (1995).

[54] A. Pfitzner, S. Reiser, and H.-J. Deiseroth, $(CuI)P_4Se_4$: An adduct of polymeric P_4Se_4 with CuI, Z. Anorgan. Allgem. Chem. **625**, 2196 (1999).

[55] G. Kresse and J. Furthmüller, Efficient iterative schemes for *ab initio* total-energy calculations using a plane-wave basis set, Phys. Rev. B **54**, 11169 (1996).

[56] G. Kresse and J. Furthmüller, Efficiency of *ab-initio* total energy calculations for metals and semiconductors using a plane-wave basis set, Comput. Mater. Sci. **6**, 15 (1996).

[57] J. P. Perdew, K. Burke, and M. Ernzerhof, Generalized gradient approximation made simple, Phys. Rev. Lett. **77**, 3865 (1996).

[58] G. Kresse and D. Joubert, From ultrasoft pseudopotentials to the projector augmented-wave method, Phys. Rev. B **59**, 1758 (1999).

[59] H. J. Monkhorst and J. D. Pack, Special points for Brillouin-zone integrations, Phys. Rev. B **13**, 5188 (1976).

[60] J. Heyd, G. E. Scuseria, and M. Ernzerhof, Hybrid functionals based on a screened Coulomb potential, J. Chem. Phys. **118**, 8207 (2003).

[61] S. Grimme, J. Antony, S. Ehrlich, and H. Krieg, A consistent and accurate *ab initio* parametrization of density functional dispersion correction (DFT-D) for the 94 elements H-Pu, J. Chem. Phys. **132**, 154104 (2010).

[62] A. Togo and I. Tanaka, First principles phonon calculations in materials science, Scr. Mater. **108**, 1 (2015).

[63] S. Nosé, A unified formulation of the constant temperature molecular dynamics methods, J. Chem. Phys. **81**, 511 (1984).

[64] D. Bucher, L. C. T. Pierce, J. A. McCammon, and P. R. L. Markwick, On the use of accelerated molecular dynamics to enhance configurational sampling in *ab initio* simulations, J. Chem. Theory Comput. **7**, 890 (2011).

[65] V. Wang, N. Xu, J. C. Liu, G. Tang, and W. Geng, VASPKIT: A user-friendly interface facilitating high-throughput computing and analysis using VASP code, Comput. Phys. Commun. **267**, 108033 (2021).

[66] K. Momma and F. Izumi, VESTA 3 for three-dimensional visualization of crystal, volumetric and morphology data, J. Appl. Crystallogr. **44**, 1272 (2011).

[67] R. Dronskowski and P. E. Bloechl, Crystal orbital hamilton populations (COHP): Energy-resolved visualization of chemical bonding in solids based on density-functional calculations, J. Phys. Chem. **97**, 8617 (1993).

[68] V. L. Deringer, A. L. Tchougreeff, and R. Dronskowski, Crystal orbital hamilton population (COHP) analysis as projected from plane-wave basis sets, J. Phys. Chem. A **115**, 5461 (2011).

[69] S. Maintz, V. L. Deringer, A. L. Tchougréeff, and R. Dronskowski, LOBSTER: A tool to extract chemical bonding from plane-wave based DFT, J. Comput. Chem. **37**, 1030 (2016).

[70] M. Yu, F. Zhang, W. Gao, H. Shen, L. Kang, L. Ju, and H. Yin, Two-dimensional $InTeClO_3$: An ultrawide-bandgap material with potential application in a deep ultraviolet photodetector, Phys. Chem. Chem. Phys. **25**, 29241 (2023).

[71] Y. Qiao, H. Shen, F. Zhang, S. Liu, and H. Yin, W_4PCl_{11} monolayer: An unexplored 2D material with moderate direct bandgap and strong visible-light absorption for highly efficient solar cells, Nanoscale **14**, 12386 (2022).

[72] S. Jiang, J. Li, W. Chen, H. Yin, G.-P. Zheng, and Y. Wang, InTeI: A novel wide-bandgap 2D material with desirable stability and highly anisotropic carrier mobility, Nanoscale **12**, 5888 (2020).

[73] F. Zhang, B. Wang, and H. Yin, Ga_3Te_3I: Novel 1D and 2D semiconductor materials with promising electronic and optical properties, J. Phys. D: Appl. Phys. **55**, 374005 (2022).

[74] L. Shulenburger, A.D. Baczewski, Z. Zhu, J. Guan, and D. Tománek, The nature of the interlayer interaction in bulk and few-layer phosphorus, Nano Lett. **15**, 8170 (2015).

[75] R. Zacharia, H. Ulbricht, and T. Hertel, Interlayer cohesive energy of graphite from thermal desorption of polyaromatic hydrocarbons, Phys. Rev. B **69**, 155406 (2004).

[76] L. Colombo and S. Giordano, Nonlinear elasticity in nanostructured materials, Rep. Prog. Phys. **74**, 116501 (2011).

[77] M. Catti, Calculation of elastic constants by the method of crystal static deformation, Acta Cryst. **41**, 494 (1985).

[78] R. C. Andrew, R. E. Mapasha, A. M. Ukpong, and N. Chetty, Mechanical properties of graphene and boronitrene, Phys. Rev. B **85**, 125428 (2012).

[79] O. H. Nielsen and R. M. Martin, First-principles calculation of stress, Phys. Rev. Lett. **50**, 697 (1983).

[80] O. H. Nielsen and R. M. Martin, Stresses in semiconductors: *Ab initio* calculations on Si, Ge, and GaAs, Phys. Rev. B **32**, 3792 (1985).

[81] Y. Le Page and P. Saxe, Symmetry-general least-squares extraction of elastic coefficients from *ab initio* total energy calculations, Phys. Rev. B **63**, 174103 (2001).

[82] V. Wang and W. T. Geng, Lattice defects and the mechanical anisotropy of borophene, J. Phys. Chem. C **121**, 10224 (2017).

[83] S. Zhang, J. Zhou, Q. Wang, X. Chen, Y. Kawazoe, and P. Jena, Penta-graphene: A new carbon allotrope, Proc. Natl. Acad. Sci. USA **112**, 2372 (2015).

[84] E. Cadelano, P. L. Palla, S. Giordano, and L. Colombo, Elastic properties of hydrogenated graphene, Phys. Rev. B **82**, 235414 (2010).

[85] A. Castellanos-Gomez, M. Poot, G. A. Steele, H. S. J. van der Zant, N. Agraït, and G. Rubio-Bollinger, Mechanical properties of freely suspended semiconducting graphene-like layers based on MoS_2, Nanoscale Res. Lett. **7**, 233 (2012).

[86] X. Shi, S. Jiang, X. Han, M. Wei, B. Wang, G. Zhao, G.-P. Zheng, and H. Yin, Ultrahigh mechanical flexibility induced superior piezoelectricity of InSeBr-type 2D Janus materials, Phys. Chem. Chem. Phys. **24**, 8371 (2022).